OPEN ACCESS

**Scholars International Journal of Chemistry and Material Sciences**

Abbreviated Key Title: Sch Int J Chem Mater Sci
ISSN 2616-8669 (Print) |ISSN 2617-6556 (Online)
Scholars Middle East Publishers, Dubai, United Arab Emirates
Journal homepage: http://saudijournals.com

**Original Research Article**

# Evaluation of Extracted Cow Bone Hydroxyapatite

Iwekumo Ebibofe Agbozu[1], Omatosan Patrick Wategire[1,2*]

[1]Department of Environmental Management and Toxicology, Federal University of Petroleum Resources, P.M.B. 1221, Effurun, Nigeria
[2]Department of Environmental Science and Management Technology, Petroleum Training Institute, P.M.B. 20, Effurun, Nigeria

**DOI:** https://doi.org/10.36348/sijcms.2025.v08i03.007 | **Received:** 05.05.2025 | **Accepted:** 10.06.2025 | **Published:** 17.06.2025

***Corresponding author:** Omatosan Patrick Wategire
Department of Environmental Management and Toxicology, Federal University of Petroleum Resources, P.M.B. 1221, Effurun, Nigeria

## Abstract

Hydroxyapatite (HAp), a calcium phosphate compound, is essential in biomedical and environmental applications due to its biocompatibility and adsorptive properties. The objectives of this study were to evaluate the compositional and structural integrity of hydroxyapatite extracted from cow femur, ribs, and skull bones by calcining the bones and analysing the resulting HAp powders using Fourier Transform Infrared Spectroscopy (FTIR), Scanning Electron Microscopy (SEM), X-ray fluorescence (XRF), and X-ray Diffraction (XRD) techniques. FTIR analysis verified the presence of distinctive phosphate and hydroxyl functional groups in all samples, indicating successful conversion to HAp. SEM micrographs showed porous, uneven surface morphologies appropriate for biointegration. XRF verified calcium and phosphorus as dominating components. The oxide composition was further confirmed by XRF analysis, which showed that the most prevalent components were calcium oxide (CaO) and phosphorus pentoxide ($P_2O_5$), but with slightly different relative proportions across bone sources. The rib sample showed a higher magnesium oxide level, whereas the skull bone sample had the greatest CaO concentration. The concentrations of the different elements in the samples were not significantly different ($p>0.05$). XRD analysis confirmed phase-pure nanocrystalline hydroxyapatite with the main (211) peak at 31.8° and crystallite sizes between 60–70 nm, indicating high crystallinity and structural consistency. These nanoscale features enhance similarity to natural bone and bioactivity. The findings show that bovine-derived HAp maintains key structural and compositional characteristics across anatomical sources, making it a practical and affordable substitute for synthetic hydroxyapatite in biomedical and environmental applications such as contaminant remediation and bone restoration.

**Keywords**: *Hydroxyapatite, Cow Bones, FTIR Spectroscopy, SEM Analysis, XRF Characterisation, XRD*.



## 1.0 INTRODUCTION

Hydroxyapatite (HAp), a calcium phosphate mineral with the chemical formula $Ca_{10}(PO_4)_6(OH)_2$, is the main inorganic component of hard tissues, especially bones and teeth, in both humans and animals [1]. Its superior biocompatibility, osteoconductivity, lack of immunogenicity, and structural resemblance to real bone mineral have attracted a lot of interest to HAp in the biomedical domain [2]. Bone grafts, dental fillings, orthopaedic coatings, maxillofacial reconstruction, and tissue engineering scaffolding are among its many applications [3]. Due to the bioactive qualities it possesses, hydroxyapatite is used in chromatography, catalysis, water purification (to remove fluoride and heavy metals), and as an additive in food and cosmetic products in addition to biomedical uses [3, 4].

Traditionally, pure chemical precursors are used to create hydroxyapatite by sol-gel, hydrothermal, wet chemical precipitation, or biomimetic processes [5]. Despite yielding high-purity HAp, these synthetic approaches can entail expensive, energy-intensive procedures and hazardous chemicals [6]. There has been a growing interest in HAp extraction from natural biowastes, particularly animal bones, because they are inexpensive, plentiful, and environmentally friendly sources [7]. Also, their high calcium phosphate concentration and accessibility as a by-product of the meat industry make bovine bones, in particular, a feasible raw material for HAp extraction [8]. In terms of crystallinity, porosity, and the presence of trace elements that improve biological performance, HAp made from cow bones is on par with or even better than synthetic HA [9]. In addition to reducing environmental impact, using bovine bone debris promotes the circular economy by converting biological waste into valuable commodities [7].

This study aimed to extract and characterise hydroxyapatite from bovine bones using thermal calcination and assess its physicochemical properties for possible biomedical and industrial applications, in light of the need for economical and sustainable substitutes for chemically synthesised hydroxyapatite.

## 2.0 METHODS

### 2.1 Sample Collection and Preparation

Following slaughter, cow bones were gathered from a nearby abattoir, placed in sterile containers, and brought to the lab for additional processing and examination. The femur, ribs, and skull were the bones that were gathered. Bones were first properly cleansed by boiling them in water for two hours to get rid of any lipids and soft tissues that might have adhered. To remove any remaining moisture, the cleaned bones were first allowed to air dry before being oven-dried for 24 hours at 105°C. To ensure consistent heat exposure, dried bones were broken up into tiny pieces using a mechanical grinder.

### 2.2 Hydroxyapatite Extraction

Hydroxyapatite was extracted following the method described previously [10]. A muffle furnace (Nabertherm LHT series) was then used to heat treat the crushed bone samples. To separate the inorganic hydroxyapatite phase and eliminate organic components, calcination was performed for one hour at 1000°C in an air environment. To avoid heat shock, the samples were calcined and then allowed to naturally cool to room temperature inside the furnace. An agate mortar and pestle were used to grind the white calcined bone material into a fine powder for additional examination.

### 2.3 Hydroxyapatite Characterisation

#### 2.3.1 Spectroscopic Analysis

The functional groups in calcined hydroxyapatite were identified using Fourier Transform Infrared Spectroscopy (FTIR) [11]. Using a hydraulic press under vacuum, 200 mg of spectroscopic-grade potassium bromide (KBr) was completely combined with about 2 mg of the powdered sample before being compressed into a translucent pellet. The sample holder of the FTIR spectrometer was then used to hold the pellet for analysis. Using 32 scans per sample to guarantee a sufficient signal-to-noise ratio, spectral data were gathered between 4000 and 650 $cm^{-1}$ at a resolution of 4 $cm^{-1}$. The formation and purity of hydroxyapatite were confirmed by identifying characteristic absorption bands that corresponded to phosphate ($PO_4^{3-}$), hydroxyl ($OH^-$), and possibly carbonate ($CO_3^{2-}$) groups.

#### 2.3.2 Surface Morphology Analysis

Scanning electron microscopy (SEM) was used to analyse the hydroxyapatite surface morphology of the sample [12]. On a carbon adhesive tape that was fastened to an aluminium stub, a tiny quantity of the calcined powder was placed. To improve conductivity and reduce charge under the electron beam, a thin layer of gold was then applied to the sample using a sputter coater. A 15 kV accelerating voltage was used for SEM imaging to get fine-grained micrographs of the particle morphology and surface structure.

#### 2.3.3 Elemental and Oxide Composition

To ascertain the elemental and oxide composition of the hydroxyapatite sample, X-ray fluorescence (XRF) spectroscopy was employed [13]. To guarantee compactness and consistent thickness, the calcined bone powder was first compressed into a pellet using a hydraulic press without the use of a binder. After that, the pellet was put into the sample chamber for examination. To increase sensitivity for light elements, measurements were made in a vacuum using a wavelength-dispersive XRF device. To guarantee accuracy, the spectrometer was calibrated using approved reference materials. Elements including calcium (Ca), phosphorus (P), magnesium (Mg), and trace metals were measured. The purity and stoichiometry extracted hydroxyapatite were revealed by the elemental data that resulted.

#### 2.3.4 Mineral Composition

To ascertain the crystalline structure and phase purity of the hydroxyapatite samples obtained from cow femur, ribs, and skull, X-ray diffraction (XRD) was employed. The calcined bone components were ground into fine particles using an agate mortar and pestle to create the powdered samples. A Bruker D8 Advance X-ray diffractometer operated at 40 kV and 40 mA and fitted with Cu-Kα radiation (λ = 1.5406 Å) was used for the analysis. At a scan rate of 1°/min and a step size of 0.02°, scans were performed throughout a 2θ range of 10° to 80°. Software was used to analyse the generated diffractograms to identify the distinctive peaks of hydroxyapatite, with reference to the ICDD database (PDF No. 09-0432). Peak sharpness and intensity were used to evaluate crystallinity, crystallite size, and phase composition. Scherrer's equation was used to get the average crystallite size from the (002) diffraction peak. Scherrer's equation is given as:

$$\tau = \frac{K\lambda}{\beta \cos\theta}$$

Where: K = 0.9 (shape factor); $\lambda$ = 0.15406nm (CU Kα radiation); β = FWHM in radians; θ = 2 θ/2; $\tau$ = crystallite size in nm

### 2.4 Data Analysis

The results obtained were presented in tables and charts. The elemental composition of the hydroxyapatite obtained from the three samples was compared using ANOVA in Microsoft Excel 2019.

## 3.0 RESULTS AND DISCUSSION

### 3.1 Spectroscopic Analysis

The results of FTIR analysis for cow femur, ribs and skull are shown in Figure 1.

The successful manufacture of hydroxyapatite from cow femur bone was indicated by the FTIR examination of the cow femur, which showed distinctive phosphate ($PO_4^{3-}$) bands around 1030–1090 $cm^{-1}$ and 560–600 $cm^{-1}$, together with hydroxyl ($OH^-$) groups near 3570 $cm^{-1}$. The structural integrity and purity of the material are confirmed by these spectrum characteristics. The hydroxyapatite FTIR spectra of cow ribs show clear absorption bands that correspond to the functional groups in the material. O-H stretching vibrations are probably the cause of the bands seen at wavenumbers above 3000 $cm^{-1}$, such as about 3630 $cm^{-1}$, which show that the hydroxyapatite contains hydroxyl groups. The presence of phosphate groups ($PO_4^{3-}$) in the 1000–1200 $cm^{-1}$ range indicates that the substance is hydroxyapatite, which is frequently seen in bone. A variety of distinctive peaks that correspond to various functional groups and bond vibrations can be seen in the hydroxyapatite FTIR (Fourier Transform Infrared) spectrum obtained from bovine skull bones. The presence of hydroxyl groups (-OH), which are crucial to the mineral structure, is shown by the large peaks seen at 3500–3700 cm-1. The nature of the hydroxyapatite is confirmed by additional peaks in the 1000–1100 $cm^{-1}$ range that are connected to phosphate ($PO4^{3-}$) vibrations. According to the findings, the sample appears to have maintained its usual crystalline form.

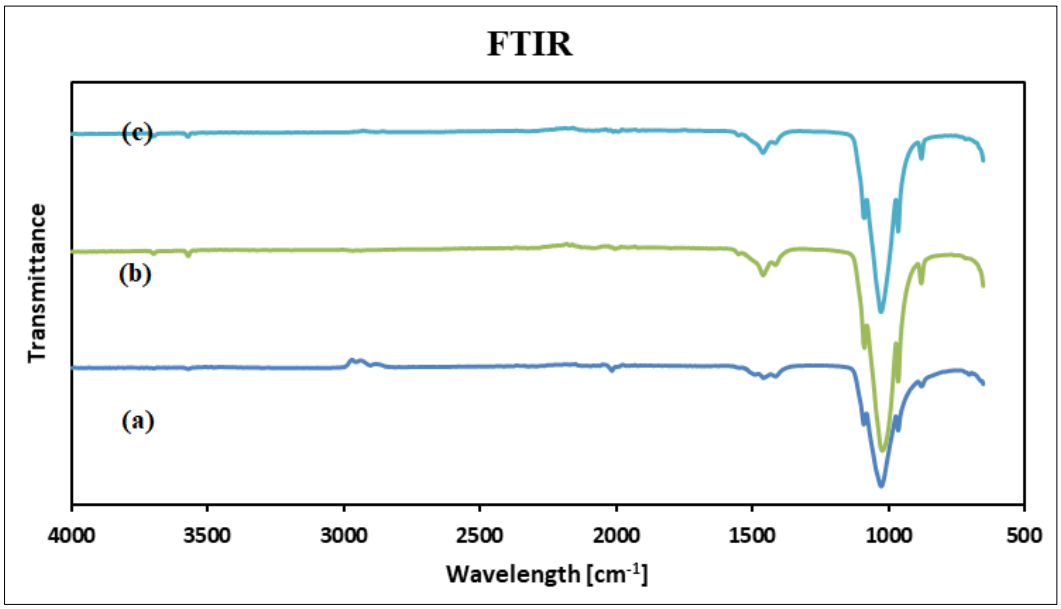


**Figure 1: FTIR spectra of Hydroxyapatite (HAp) derived from cow bone. (a) Cow Femur; (b) Cow Rib; (c) Cow Skull**

The variations in the mineral and organic compositions of the skull, ribs, and femur were evaluated by comparing their FTIR spectra. Similar hydroxylation in the hydroxyapatite structures of the three samples was suggested by the broad peak around 3500-3700 $cm^{-1}$, which is indicative of hydroxyl groups (O-H stretch) similar to those found in [14], and [15]. Additionally, there was a band at about 1650 $cm^{-1}$ that was linked to H-O-H bending and indicated bound water; the intensity of this band varied little across the samples. The existence of hydroxyapatite was indicated by the prominent bands located between 1021 – 1088 cm-1, 965 cm-1 and 652 cm-1 in all three samples are allocated to the Phosphate ($PO_4^{3-}$) asymmetric stretching vibration ($v_3$), Phosphate ($PO_4^{3-}$) symmetric stretching vibration ($v_1$) and phosphate ($PO_4^{3-}$) bending vibration ($v_4$) respectively [16, 17]. But the disparities in peak positions and intensities might indicate different mineral crystallinity. There were also carbonate bands at about 1400–1450 $cm^{-1}$ and 870 $cm^{-1}$, albeit their intensities differed, which might have been caused by variations in the carbonate substitution in the hydroxyapatite [18]. A Silicate ion vibration mode ($SiO_4^{4-}$) was found at 880 cm-1 [19], and was confirmed by the XRF result showing an elemental average of 1.241% and an oxide average of 2.654% in all three samples. Although a possible HA contamination, as zero report has shown silicate as a constituent of a cow bone-derived HA. The silicate ion contamination may have resulted from residual silica fumes (vapourized silicon dioxide from oxidation reaction) in the electric furnace used during calcination [20]. It was also reported that the inner lining fire blocks of electrical furnaces are often made up of silica-based compounds like silicate carbide (SiC), quartz ($SiO_2$) and calcium silicate ($CaSiO_3$) because of their ability to withstand very high temperatures without disintegrating [21, 22].

### 3.2 Surface Morphology

The results of sample analysis using SEM are shown in Figure 2 (Cow femur, rib and skull), which shows that it is a bit amorphous in shape but largely resembles spherical particles. The spherical shape seen in Figure 2 aligned with what was observed by Dom *et al*., (2024). A synthesized hydroxyapatite obtained from cow bone was characterized. Furthermore, the edges of

the samples as observed by the SEM micrograph, were not well-defined but looked rounded and agglomerated well to form much larger aggregate structures of multiple independent clusters. It is also quite visible that the particles suggest a notable prevalence of rough, well-developed porous surfaces with visible fissures as a possible result of their calcination at high temperature [23, 24]. The increased number of pores and crevasses is a result of the conversion of organic matter, which was initially present between 30 to 40%, to gases, particularly $CO_2$, during the calcination process [25, 26].

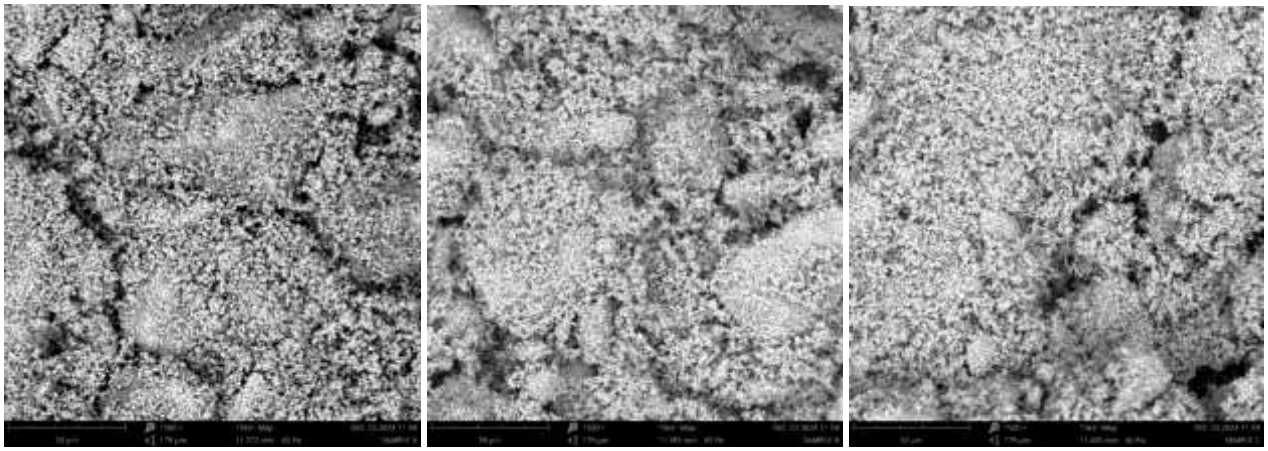

a b c

**Figure 2: Scanning Electron Micrograph (SEM) image of Hydroxyapatite (HAp) derived from cow bone. (a) Cow Femur; (b) Cow Rib; (c) Cow Skull**

### 3.3 Elemental and Oxide Composition

Table 1 to 3 shows the results of the XRF analysis of hydroxyapatite from the samples.

A complicated oxide composition was discovered through elemental analysis of hydroxyapatite from a cow femur (Table 1). With the highest weight (62.976 wt.%) percentage and quantitative computations showed that calcium oxide (CaO) was the predominant component. Phosphorus pentoxide ($P_2O_5$) constituted the second most prevalent component (28.879 wt.%). Lower but detectable amounts of silicon dioxide ($SiO_2$) and aluminium oxide ($AlO_3$) were found. Trace levels of chlorine and several other metal oxides were found, each with a different level of analytical error.

**Table 1: Elemental analysis from XRF for cow femur**

| Element | % Element | Oxide | % Oxide |
|---|---|---|---|
| O | 37.617 | - | - |
| Mg | 0.000 | MgO | 0.000 |
| Al | 1.735 | $Al_2O_3$ | 3.278 |
| Si | 1.334 | $SiO_2$ | 2.854 |
| P | 12.604 | $P_2O_5$ | 28.879 |
| S | 0.061 | $SO_3$ | 0.151 |
| Cl | 0.787 | Cl | 0.787 |
| K | 0.031 | $K_2O$ | 0.037 |
| Ca | 45.010 | CaO | 62.976 |
| Ti | 0.008 | $TiO_2$ | 0.014 |
| V | 0.002 | $V_2O_5$ | 0.003 |
| Cr | 0.001 | $Cr_2O_3$ | 0.001 |
| Mn | 0.027 | MnO | 0.035 |
| Fe | 0.137 | $Fe_2O_3$ | 0.196 |
| Co | 0.009 | CoO | 0.011 |
| Ni | 0.004 | NiO | 0.005 |
| Cu | 0.029 | CuO | 0.037 |
| Zn | 0.006 | ZnO | 0.007 |
| Rb | 0.002 | $Rb_2O$ | 0.003 |
| Sr | 0.067 | SrO | 0.079 |
| Zr | 0.001 | $ZrO_2$ | 0.001 |
| Nb | 0.010 | $Nb_2O_5$ | 0.015 |

| Element | % Element | Oxide | % Oxide |
|---|---|---|---|
| Ag | 0.023 | $Ag_2O$ | 0.025 |
| Sn | 0.316 | $SnO_2$ | 0.401 |
| Cs | 0.000 | $Cs_2O$ | 0.000 |
| Ba | 0.141 | BaO | 0.158 |
| Ta | 0.025 | $Ta_2O_5$ | 0.031 |
| W | 0.007 | $WO_3$ | 0.009 |
| Pb | 0.005 | PbO | 0.006 |

Calcium oxide (CaO) is the main component, according to quantitative XRF analysis of the hydroxyapatite sample. It has the highest concentration in weight (60.749 wt.%). The second most prevalent component, phosphorus pentoxide ($P_2O_5$), has a weight percentage of 28.869. Significantly, there is a higher trace level of magnesium oxide (MgO) detected (3.261 wt.%). Aluminium oxide ($AlO_3$) and silicon dioxide ($SiO_2$) are also found in trace amounts. Additionally, trace amounts of chloride and other oxides are noted.

**Table 2: Elemental analysis from XRF for cow ribs**

| Element | % Element | Oxide | % Oxide |
|---|---|---|---|
| O | 37.728 | - | - |
| Mg | 1.967 | MgO | 3.261 |
| Al | 1.008 | $Al_2O_3$ | 1.904 |
| Si | 1.380 | $SiO_2$ | 2.952 |
| P | 12.599 | $P_2O_5$ | 28.869 |
| S | 0.044 | $SO_3$ | 0.110 |
| Cl | 0.844 | Cl | 0.844 |
| K | 0.130 | $K_2O$ | 0.156 |
| Ca | 43.418 | CaO | 60.749 |
| Ti | 0.025 | $TiO_2$ | 0.041 |
| V | 0.017 | $V_2O_5$ | 0.031 |
| Cr | 0.000 | $Cr_2O_3$ | 0.000 |
| Mn | 0.026 | MnO | 0.033 |
| Fe | 0.273 | $Fe_2O_3$ | 0.390 |
| Co | 0.004 | CoO | 0.005 |
| Ni | 0.001 | NiO | 0.001 |
| Cu | 0.028 | CuO | 0.035 |
| Zn | 0.006 | ZnO | 0.008 |
| Rb | 0.002 | $Rb_2O$ | 0.002 |
| Sr | 0.066 | SrO | 0.078 |
| Zr | 0.005 | $ZrO_2$ | 0.007 |
| Nb | 0.006 | $Nb_2O_5$ | 0.008 |
| Ag | 0.025 | $Ag_2O$ | 0.027 |
| Sn | 0.266 | $SnO_2$ | 0.338 |
| Cs | 0.008 | $Cs_2O$ | 0.009 |
| Ba | 0.091 | BaO | 0.101 |
| Ta | 0.011 | $Ta_2O_5$ | 0.014 |
| W | 0.008 | $WO_3$ | 0.010 |
| Pb | 0.013 | PbO | 0.014 |

Calcium oxide (CaO) makes up a significant 66.683 wt.% of the hydroxyapatite obtained from cow skulls, according to XRF analysis, which also shows little analytical error. Its second largest component is phosphorus pentoxide ($P_2O_5$) (26.571 wt.%). There is also a trace amount of silicon dioxide ($SiO_2$) and aluminium oxide ($AlO_3$). Several additional oxides are found in trace amounts, such as vanadium, manganese, chromium, iron, cobalt, nickel, copper, niobium, tungsten, barium, tantalum, titanium, zinc, silver, tin, lead, rubidium, caesium, strontium, and chloride. The elemental profile of the hydroxyapatite sample under analysis is provided by the measured weight and mole percentages and their corresponding errors.

**Table 3: Elemental analysis from XRF for cow skull**

| Element | % Element | Oxide | % Oxide |
|---|---|---|---|
| O | 36.513 | - | - |
| Mg | 0.000 | MgO | 0.000 |
| Al | 1.121 | $Al_2O_3$ | 2.118 |
| Si | 1.009 | $SiO_2$ | 2.158 |
| P | 11.596 | $P_2O_5$ | 26.571 |
| S | 0.066 | $SO_3$ | 0.164 |
| Cl | 1.101 | Cl | 1.101 |
| K | 0.030 | $K_2O$ | 0.036 |
| Ca | 47.659 | CaO | 66.683 |
| Ti | 0.027 | $TiO_2$ | 0.045 |
| V | 0.014 | $V_2O_5$ | 0.025 |
| Cr | 0.000 | $Cr_2O_3$ | 0.000 |
| Mn | 0.029 | MnO | 0.037 |
| Fe | 0.173 | $Fe_2O_3$ | 0.247 |
| Co | 0.009 | CoO | 0.012 |
| Ni | 0.005 | NiO | 0.007 |
| Cu | 0.033 | CuO | 0.042 |
| Zn | 0006 | ZnO | 0.007 |
| Rb | 0.002 | $Rb_2O$ | 0.002 |
| Sr | 0.071 | SrO | 0.083 |
| Zr | 0.001 | $ZrO_2$ | 0.001 |
| Nb | 0.006 | $Nb_2O_5$ | 0.009 |
| Ag | 0.021 | $Ag_2O$ | 0.022 |
| Sn | 0.387 | $SnO_2$ | 0.492 |
| Cs | 0.010 | $Cs_2O$ | 0.011 |
| Ba | 0.073 | BaO | 0.082 |
| Ta | 0.019 | $Ta_2O_5$ | 0.023 |
| W | 0.006 | $WO_3$ | 0.008 |
| Pb | 0.013 | PbO | 0.014 |

The comparison of the composition of the hydroxyapatite obtained from the femur, ribs and skull bones using ANOVA (Table 4) shows that there was no significant difference between the various concentrations of different elements present in the three samples ($p>0.05$).

**Table 4: ANOVA Comparison of Composition of Hydroxyapatite from Cow Bone**

| *Source of Variation* | *SS* | *df* | *MS* | *F* | *P-value* | *F crit* |
|---|---|---|---|---|---|---|
| Between Groups | 1.67E-07 | 2 | 8.33E-08 | 5.02E-10 | 1 | 3.109311 |
| Within Groups | 13459.56 | 81 | 166.1674 | | | |
| Total | 13459.56 | 83 | | | | |

The XRF analysis revealed that calcium oxide (CaO) and phosphorus pentoxide ($P_2O_5$) were the dominant oxides in all samples, consistent with hydroxyapatite (HAp) composition. However, calcium concentrations were lower than the theoretical purity of synthetic HAp. This deviation is attributed to the biological origin of the bone, which contains organic matter, water, and substituted ions [27]. Anatomical variation also plays a role; for instance, skull bones may contain more organic material than load-bearing femur bones [10]. Additionally, elemental substitution—with $Mg^{2+}$, $Na^{+}$, and $Zn^{2+}$ replacing $Ca^{2+}$ in the lattice—lowers calcium percentages while maintaining biofunctionality [28]. Finally, trace oxides such as $Al_2O_3$, $SiO_2$, and others may result from the animal's diet, environment, or contamination during processing [29].

**3.4 Mineral Composition**

Figure 3 shows the results of the XRD analysis of the hydroxyapatite from cow femur, ribs and skull bones.

As shown in Figure 3 (a), the characteristic peaks that match the standard JCPDS card no. 09-0432 in the XRD examination verifies the existence of crystalline hydroxyapatite (HA). The primary crystal orientation of HAp is indicated by the strongest peak at $2\theta = 31.78°$, which corresponds to the (211) plane. Phase purity is confirmed by further notable peaks at 25.88°, 28.63°, 32.22°, and 32.91°, which correlate to additional

HAp planes. These peaks' strength and sharpness suggest high crystallinity. The (211) plane's crystallite size was determined using the Scherrer equation to be roughly 60 nm, indicating nanoscale crystallites appropriate for.

Diffraction peaks in the XRD pattern that match the standard JCPDS card number. 09-0432 shows that crystalline hydroxyapatite (HAp) has formed. As is typical of HAp, the most intense peak is seen at 2θ = 31.85°, which corresponds to the (211) plane. The phase identification is supported by further peaks at 25.93°, 29.03°, 32.25°, and 32.96°, which correspond to the (002), (210), (112), and (300) planes, respectively. The high relative intensities and crisp, narrow peaks indicate a well-crystallized structure. The crystallite size was estimated to be around 70 nm using the Scherrer equation on the most intense (211) signal, indicating nanoscale HA particles.

The diffraction peaks in the XRD measurements closely match those of standard hydroxyapatite (HAp) (JCPDS card no. 09-0432), confirming the development of crystalline HAp. The (211) plane, which is the distinctive signature of HAp, is shown by the most dramatic peak at 2θ = 31.85°. Phase purity is supported by further prominent peaks at 25.96°, 29.01°, 32.25°, and 32.97°, which are ascribed to the (002), (210), (112), and (300) planes, respectively. A well-crystallized structure is indicated by the high relative intensities and distinct, sharp peaks. Based on the FWHM of the (211) peak and the Scherrer equation, the estimated crystallite size is roughly 63 nm, indicating a nanocrystalline structure.

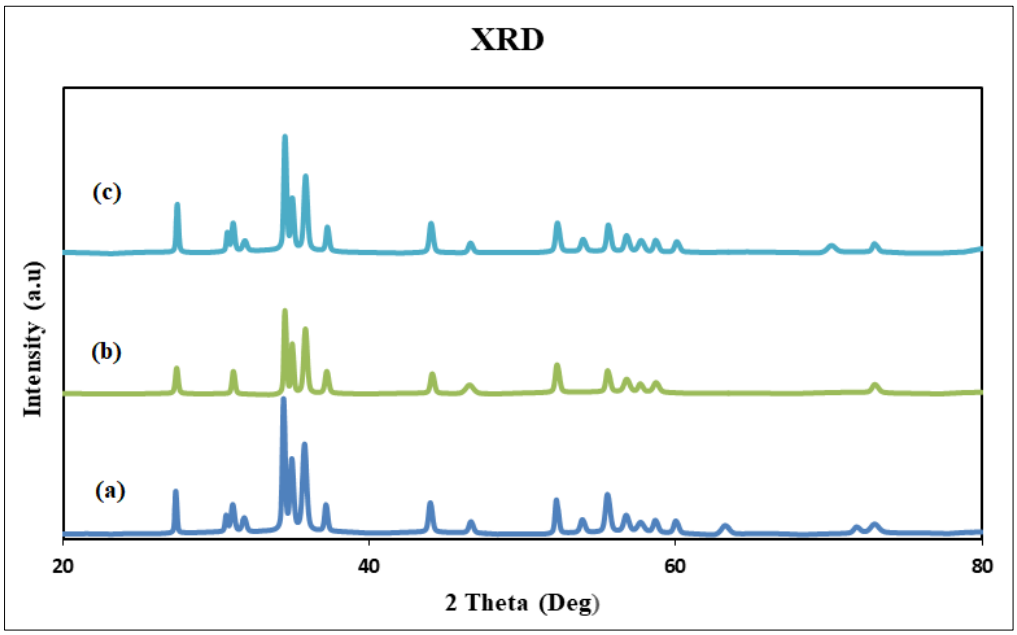


**Figure 3: XRD readout of Hydroxyapatite (HAp) derived from cow bone. (a) Cow Femur; (b) Cow Rib; (c) Cow Skull**

As shown in figure 4, hatrurite, which is a tricalcium silicate mineral ($Ca_3SiO_5$) and Quartz ($SiO_2$), which was seen as the secondary phase of the produced hydroxyapatite in all three cow bone samples (although at different concentrations), were possibly formed during the calcination period in the electric furnace having a silica-based lining.

$$Ca_{10}(PO_4)_6(OH)_{2\,(s)} \rightarrow 3Ca_3(PO_4)_{2\,(s)} + CaO_{\,(s)} + H_2O_{\,(g)} \quad (3.1)$$

At calcination temperatures above 600°C HAp is reported to disintegrate to β-tricalcium phosphate (β-TCP) and calcium oxide (CaO) as shown in the reaction above [38, 39]. Therefore, two possible reactions may have occurred, leading to the formation of tricalcium silicate.

$$3CaO_{(s)} + SiO_{2\,(s)} \rightarrow Ca_3SiO_{5\,(s)} \quad (3.2)$$

$$3Ca(OH)_{2\,(s)} + SiO_{2\,(s)} \rightarrow Ca_3SiO_{5\,(s)} + 2H_2O_{\,(g)} \quad (3.3)$$

The particular reaction is a solid-state process in which tricalcium silicate is created when calcium oxide (CaO) and silica ($SiO_2$) mix at elevated temperatures [30, 31]. These silica particles reacting with CaO are submicron vapour-like residuals from the oxidation of the silica-based electric furnace lining [20].

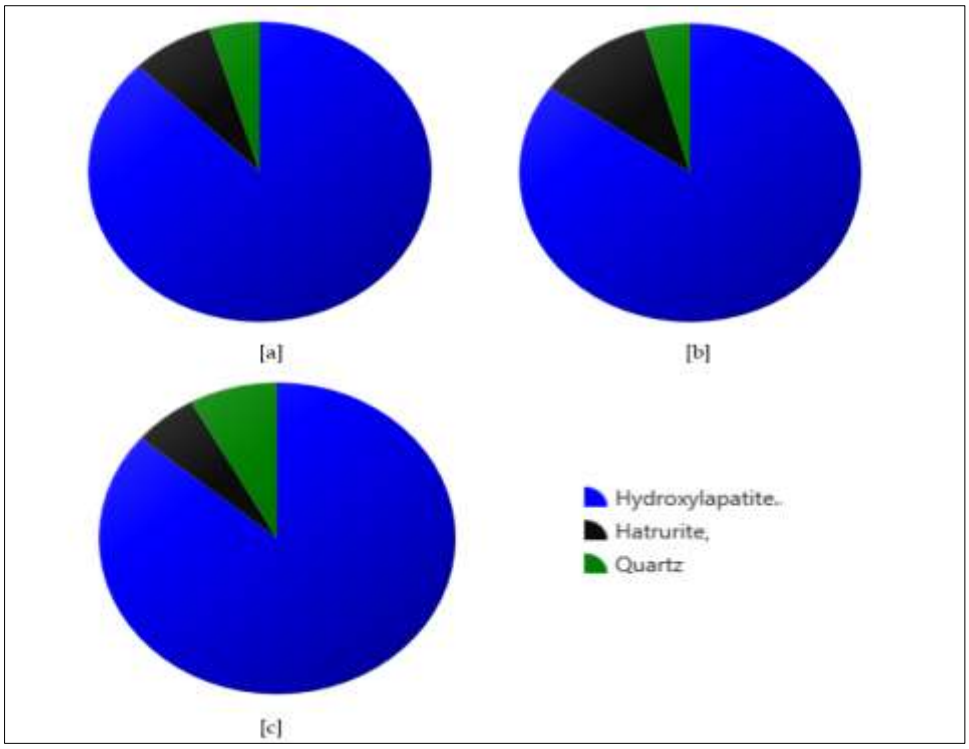


**Figure 4: Pie Chart Showing the Mineral Content Percentage of Cow Bone. (a) Cow Femur; (b) Cow Rib; (c) Cow Skull**

Using FTIR, SEM, XRF, and XRD techniques, the thorough characterisation of hydroxyapatite generated from cow femur, ribs, and skull bones emphasises compositional and morphological differences while confirming the typical properties of extracted hydroxyapatite [32]. The presence of crystalline hydroxyapatite is confirmed by the presence of distinctive phosphate ($PO_4^{3-}$) and hydroxyl ($OH^-$) vibrational bands in all the FTIR spectra, in line with [33]. Variations in crystallinity or the presence of trace elements influencing local chemical environments are suggested by slight variations in peak intensities and positions. All three samples have surface morphologies with asymmetrically formed, irregularly sized particles with random orientation, and this is in agreement with [14]. The different grey tones that show variations in particle orientation and light reflectance give the textures the appearance of being porous and lacking structural fusion. These characteristics suggest a high surface area-to-volume ratio, which is characteristic of precipitation-produced hydroxyapatite [34]. Due to its increased reactivity and adsorption capability, this shape is beneficial for applications in environmental and biomedical cleanup [35].

Calcium and phosphorus are confirmed to be the predominant elements by XRF elemental profiling, with notable contributions from nitrogen, sodium, magnesium, aluminium, and trace amounts of other metals [36]. While the rib sample had higher magnesium levels, the skull sample contained higher levels of zinc and nitrogen. These variations imply site-specific trace element incorporation, which is probably impacted by physiological function [17]. These results are supported by XRF oxide composition analysis, which shows that CaO and $P_2O_5$ are the main constituents in all samples, as in previous studies [14]. The femur and ribs had somewhat greater $P_2O_5$ contents, but the skull sample had the greatest CaO level. These variances also show how different bone forms differ in their mineralisation and assimilation of elements [34].

The effective manufacture of nanocrystalline hydroxyapatite (HAp) is confirmed by the XRD data for all samples. The main (211) peak at 31.8° and other diffraction peaks match the typical HAp pattern. High crystallinity is shown by the sharpness and intensity of the peaks, and the nanoscale nature of the material is confirmed by the estimated crystallite sizes, which range from 60 to 70 nm. Phase purity, which is essential for biomedical applications including drug delivery, implant coatings, and bone restoration, is implied by the lack of secondary phases [37]. Compared to microcrystalline forms, nanocrystalline HAp more closely resembles the mineral component of natural bone, improving osseointegration and bioactivity [28]. Good synthesis control and repeatability are also suggested by the constant structural integrity of the samples. These qualities demonstrate the material's potential for use in regenerative medicine as a biocompatible and bioactive agent.

## 4.0 CONCLUSION

This study successfully characterizes hydroxyapatite (HAp) produced from cow femur, ribs, and skull bones. The results verify that every sample maintained the fundamental structural and chemical

characteristics of hydroxyapatite, such as the existence of strong phosphate and hydroxyl groups, which denotes the purity of the material. While calcium and phosphorus were found to be the predominant constituents by elemental and oxide analyses. The skull exhibits the highest calcium content, showing the anatomical influence on mineral composition. Although the concentrations of the different elements in the samples were not significantly different ($p>0.05$). These compositional changes may affect the physicochemical and biological performance of the HAp. The extracted hydroxyapatite is a great option for biomedical and environmental uses, including bone grafting and pollutant removal, providing an affordable and environmentally friendly substitute for manufactured materials.

**Data Availability:** The authors declare that the data supporting the findings of this study are available within the paper

**DECLARATIONS**

**Competing Interests:** Authors have declared that no competing interests exist.

## REFERENCES


1. Arokiasamy P, Abdullah MMAB, Abd Rahim SZ, Luhar S, Sandu AV, Jamil NH, Nabiałek M (2022) Synthesis methods of hydroxyapatite from natural sources: A review. Ceram Int 48:14959–14979. https://doi.org/10.1016/j.ceramint.2022.03.064
2. Mondal S, Park S, Choi J, Vu TTH, Doan VHM, Vo TT, Oh J (2023) Hydroxyapatite: a journey from biomaterials to advanced functional materials. Adv Colloid Interface Sci 321:103013. https://doi.org/10.1016/j.cis.2023.103013
3. Fiume E, Magnaterra G, Rahdar A, Verné E, Baino F (2021) Hydroxyapatite for biomedical applications: A short overview. Ceramics 4:542–563. https://doi.org/10.3390/ceramics4040039
4. Kareem RO, Bulut N, Kaygili O (2024) Hydroxyapatite biomaterials: a comprehensive review of their properties, structures, medical applications, and fabrication methods. J Chem Rev 6:1–26
5. Jemli YE, Abdelouahdi K, Minh DP, Barakat A, Solhy A (2022) Synthesis and characterization of hydroxyapatite and hydroxyapatite-based catalysts. In: Design and Applications of Hydroxyapatite-Based Catalysts. Wiley, pp 19–72. https://doi.org/10.1002/9783527830190.ch2
6. Devesa S, Benzarti Z, Soreto S, Carvalho S (2025) Sol-gel synthesis of hydroxyapatite: applications, methods, and a case study. https://doi.org/10.5772/intechopen.1009779
7. Adhikara AG, Maharani AP, Puspitasari A, Nuswantoro NF, Juliadmi D, Maras MAJ, Saksono B (2024) Bovine hydroxyapatite for bone tissue engineering: preparation, characterization, challenges, and future perspectives. Eur Polym J 214:113171. https://doi.org/10.1016/j.eurpolymj.2024.113171
8. Moradi A, Pakizeh M, Ghassemi T (2021) A review on bovine hydroxyapatite; extraction and characterization. Biomed Phys Eng Express 8:012001
9. Luthfiyah S, Soegijono B, Susetyo FB, Notonegoro HA (2022) Comparing properties of bovine bone derived hydroxyapatite and synthetic hydroxyapatite. J Appl Sci Eng 25:1197–1203
10. Dorozhkin SV (2010) Bioceramics of calcium orthophosphates. Biomaterials 31:1465–1485. https://doi.org/10.1016/j.biomaterials.2009.11.050
11. Paital SR, Dahotre NB (2009) Calcium phosphate coatings for bio-implant applications: materials, performance factors, and methodologies. Mater Sci Eng R Rep 66:1–70. https://doi.org/10.1016/j.mser.2009.04.001
12. Mourino V, Cattalini JP, Boccaccini AR (2012) Metallic ions as therapeutic agents in tissue engineering scaffolds: an overview of their biological applications and strategies for new developments. J R Soc Interface 9:401–419. https://doi.org/10.1039/9781849737619-00001
13. Wopenka B, Pasteris JD (2005) A mineralogical perspective on the apatite in bone. Mater Sci Eng C 25:131–143. https://doi.org/10.1016/j.msec.2005.01.008
14. Bano N, Jikan SS, Basri H, Adzila S, Zago DM (2019) XRD and FTIR study of A&B type carbonated hydroxyapatite extracted from bovine bone. AIP Conf Proc 2068:1
15. Ghosh T, Das A, Saha P, Mishra S (2023) FTIR and XRD characterization of hydroxyapatite from biological sources. RSC Adv 13:4550–4560. https://doi.org/10.1039/d3ra07556g
16. Jamil M, Elouatli B, Khallok H, Elouahli A, Gourri E, Ezzahmouly M, Abida F, Hatim Z (2018) Silicon substituted hydroxyapatite: preparation with solid-state reaction, characterization and dissolution properties. J Mater Environ Sci 9:2322–2327.
17. Mahabole MP, Lakhane MA, Choudhari AL, Khairnar RS (2023) Structural characterization and mineralization behavior of hydroxyapatite synthesized from natural sources. J Biomater Nanobiotechnol 14:156–165. https://doi.org/10.4236/jbnb.2023.145011
18. Ali SA, Alkhateeb H, Khan A (2023) Spectroscopic and structural investigation of synthetic hydroxyapatite and comparison with biological apatite. Mater 16:4010
19. Ratnayake J, Ramesh N, Gould ML, Mucalo MR, Dias GJ (2024) Silicate-substituted bovine-derived hydroxyapatite as a bone substitute in regenerative dentistry. J Appl Biomater Funct Mater. https://doi.org/10.1177/22808000251314302
20. Sanjuán MÁ, Argiz C, Gálvez JC, Moragues A (2015) Effect of silica fume fineness on the improvement of Portland cement strength

performance. Constr Build Mater 96:55–64. https://doi.org/10.1016/j.conbuildmat.2015.07.092
21. Mombelli D, Mapelli C, Barella S, Gruttadauria A, Le Saout G, Garcia-Diaz E (2014) The efficiency of quartz addition on electric arc furnace (EAF) carbon steel slag stability. J Hazard Mater 279:586–596. https://doi.org/10.1016/j.jhazmat.2014.07.045
22. Wang Y, Chuang Y, Lin C (2015) The performance of calcium silicate board partition fireproof drywall assembly with junction box under fire. Adv Mater Sci Eng 2015:1–12. https://doi.org/10.1155/2015/642061
23. Olaoye R, Afolayan O, Adeyemi KA, Ajisope LO, Adekunle OS (2020) Adsorption of selected metals from cassava processing wastewater using cow-bone ash. Sci Afr 10:e00653. https://doi.org/10.1016/j.sciaf.2020.e00653
24. Dom AHM, Rezadin S, Rahim TA, Shamsudin Z, Shamsuri RS, Alhamoudi FH (2024) Influence of calcination temperature on the physicochemical properties of synthesized hydroxyapatite from cow bone waste. J Adv Res Micro Nano Eng 23:115–127. https://doi.org/10.37934/armne.23.1.115127
25. Luna-Zaragoza D, Romero-Guzman ET, Gutierrez-Reyes RL (2009) Surface and physicochemical characterization of phosphates Vivianite, Fe2(PO4)3 and hydroxyapatite, Ca5(PO4)3OH. J Miner Mater Charact Eng 8:591–609. https://doi.org/10.4236/jmmce.2009.88052
26. Ulakpa CW, Adaeze IM, Chimezie OA, Olaseinde AA, Odeworitse E, Onoriode E, Sarafa OA, Olutoye MA, Dim P, Siddique M (2024) Synthesis and characterization of calcium oxide nanoparticles (CaO NPs) from snail shells using hydrothermal method. J Turk Chem Soc A Chem 11:825–834. https://doi.org/10.18596/jotcsa.1416214
27. Koutsopoulos S (2002) Synthesis and characterization of hydroxyapatite crystals: a review study on the analytical methods. J Biomed Mater Res 62:600–612
28. Verma G, Quadros M (2024) Hydroxyapatite nanostructured materials for biomedical applications. In: Engineered Biomaterials: Progress and Prospects, pp 229–258
29. Horta M K dos S, Westin C, da Rocha D N, de Campos J B, de Souza R F M, Aguilar M S, Moura F J (2023) Hydroxyapatite from biowaste for biomedical applications: Obtainment, characterization and in vitro assays. Mater Res 26:e20220466. https://doi.org/10.1590/1980-5373-MR-2022-0466
30. Nicoleau L, Nonat A, Perrey D (2013) The di- and tricalcium silicate dissolutions. Cem Concr Res 47:14–30. https://doi.org/10.1016/j.cemconres.2013.01.017
31. Ashraf W, Olek J, Atakan V (2015) A comparative study of the reactivity of calcium silicates during hydration and carbonation reactions. 14th Int Congr Chem Cem (ICCC 2015), Beijing, China.
32. Liu Y, Zhang L, Wang X (2023) Structural and morphological analysis of bovine hydroxyapatite for biomedical applications. J Mater Sci 58(7):2412–2422. https://doi.org/10.1007/s10853-023-07676-9
33. Zhang Y, Li J, Wang H, Zhou Z (2022) Spectroscopic analysis of bone-derived hydroxyapatite and its protein interactions. Int J Mol Sci 23(24):15234. https://doi.org/10.3390/ijms232415234
34. Youness R A, Taha M A (2024) Tuning biodegradability, bone-bonding capacity, and wear resistance of zinc-30% magnesium intermetallic alloy for use in load-bearing bone applications. Sci Rep 14:2425. https://doi.org/10.1038/s41598-024-52648-6
35. Zhou Y, Yang S, Zhang S (2023) Hydroxyapatite from animal bones: A review of synthesis methods, characterisation, and biomedical applications. J Mater Chem B 11(5):992–1010. https://doi.org/10.1039/D3TB01395D
36. Ellingham S T D, Thompson T J U, Islam M (2018) Scanning electron microscopy-energy-dispersive X-ray (SEM/EDX): A rapid diagnostic tool to aid the identification of burnt bone and contested cremains. J Forensic Sci 63(2):504–510. https://doi.org/10.1111/1556-4029.13541
37. Dorozhkin S V (2009) Calcium orthophosphates in nature, biology and medicine. Mater 2(2):399–498.
38. Liao C, Lin F, Chen K, Sun J (1999) Thermal decomposition and reconstitution of hydroxyapatite in air atmosphere. Biomaterials 20(19):1807–1813. https://doi.org/10.1016/S0142-9612(99)00076-9
39. Ou S, Chiou S, Ou K (2013) Phase transformation on hydroxyapatite decomposition. Ceram Int 39(4):3809–3816. https://doi.org/10.1016/j.ceramint.2012.10.221